Correlation of microstructural and mechanical properties of neutron irradiated EUROFER97 steel

M. Klimenkov*, U. Jäntsch, M. Rieth, A. Möslang

Karlsruhe Institute of Technology (KIT), Institute for Applied Materials - Applied Materials Physics (IAM-AWP), Hermann-von-Helmholtz-Platz 1, 76344 Eggenstein-Leopoldshafen, Germany

*Corresponding author: michael.klimenkov@kit.edu

Telephone number: +49 721 608 22903

Fax number: +49 721 608 24567

E-mail address: michael.klimenkov@kit.edu

Abstract:

The reduced activation ferritic-martensitic (RAFM) steel EUROFER97 was neutron irradiated to an average dose of 16.3 dpa at temperatures from 250°C to 415°C. Radiation-induced defects such as dislocation loops and voids were characterized by transmission electron microscopy (TEM). The quantitative analysis of the microstructural results includes the determination of the Burgers vector, the size, number density of defects and the calculation of the relaxation volume of the loops or void swelling. The dislocation loops with b<100> Burgers vector were found in the material irradiated at 250°C and 300°C, while at higher temperatures a preferential formation of b<100> loops was observed. The voids were found only in material irradiated at 350°C and 400°C. The maximum relaxation volume of the loops and void swelling was measured for 350°C. The dispersed barrier hardening (DBH) model was found to accurately predict the yield strength in the material irradiated at the temperatures ≥350°C. The difference between experiment and DBH model at lower temperatures is due to the formation of nano-voids or interstitial loops with a size of <2nm that are not recognizable in the TEM.

Keywords: Neutron irradiation, EUROFER97, dislocation loops, bubbles, transmission electron microscopy, TEM

1. Introduction

Reduced activation materials, which show high radiation resistance, are required for the planning, construction, and a reliable operation of environment-friendly fusion power plants. The reduced activation ferritic-martensitic (RAFM) steel EUROFER97 was systematically developed for this purpose in Europe [1–5]. Industrial batches of meanwhile more than 20 tons were produced by different EU companies with a variety of different heat and semi-finished products, quality assured product forms (forged bars, plates, tubes, wires) in different dimensions. Despite many favourable properties of EUROFER97 steel, an intrinsic issue of 9% Cr-steels is the irradiation-induced hardening and embrittlement below irradiation temperatures of 400°C and specifically the pronounced strain localization in tensile tests at temperatures between 250 °C and 400 °C [6]. The materials database includes, besides the qualification of unirradiated base and joined materials [2], also a broad range of neutron irradiation data [7–9]. As part of the latter, mixed spectrum irradiations in the HFR Petten reactor have been performed on EUROFER97 [10] and results of new investigations on samples from this irradiation campaign are presented and discussed in the present paper.

In general, dislocation structures with both $\boldsymbol{b}\langle 100\rangle$ and $\boldsymbol{b}\frac{1}{2}\langle 111\rangle$ Burgers vectors are formed in EUROFER97 under neutron irradiation. The numerous studies show the strong dependence of irradiation temperature on their characteristics [11–13]. It was shown that below 350°C majority of defects are formed as featureless “black dots”, influencing decisive degradation of mechanical properties [6,12]. Hardening is understood to arise due to the formation of voids, precipitates, and/or dislocation loops with both $\boldsymbol{b}\langle 100\rangle$ and $\frac{1}{2}b\langle 111\rangle$ Burgers vectors. In any case, microstructural investigations of irradiated material are essential to understand the radiation-induced changes in mechanical properties and to predict the performance of structural compounds under real conditions. The detailed characterization of induced defects occurring at different irradiation temperatures, the determination of their type, size, spatial distribution and other parameters can make a decisive contribution to the reactor design. Finally, such a dislocation loop analysis will certainly contribute to the experimental validation of computer simulation methods.

This paper presents a TEM study of microstructural changes in EUROFER97 samples irradiated at up to 18.1 dpa in the 250-420°C temperature range. Special attention was given to the temperature dependence of the irradiation-induced loop density in order to better understand the recently observed temperature-dependent hardening and embrittlement

behavior.

2. Experimental

2.1. Materials and specimen preparation

The EUROFER97 steel investigated in the present study was produced by Böhler Austria GmbH with a chemical composition of 8.91 Cr, 0.48 Mn, 0.2 V, 0.1Ta, 0.12 C in wt%. The material was austenitized at 980°C/0.5h and subsequently tempered at 760°C/1.5h at the steel plant prior to delivery.

The irradiation was performed in the HFR (High Flux Reactor, Petten, Netherlands) with an average neutron flux of 3.99 x 10^{18} $m^{-2}s^{-1}$ (E>0.1 MeV). Impact test specimens have been irradiated to the average dose of 16.3±1.9 dpa at the targeted irradiation temperatures of 250°C, 300°C, 350°C, 400°C and 450 °C. The targeted and measured temperatures as well as damage dose for each temperature are shown in Tab.1. Since the target and average temperatures are within the error range, we use the target temperature when discussing the results. The only exception was the samples irradiated at 450°C, where the average temperature showed significantly higher deviation from targeted value. Further in the manuscript, the 415°C temperature is used to discuss radiation-induced defects in the material irradiated at the target temperature of 450°C. Detailed information on the irradiation program and on material properties of the used EUROFER97 heat can be found in [10].

Targeted temperature /°C	250	300	350	400	450
Average temperature /°C	252±8	293±8	347±7	392±8	413±21
Damage dose /dpa	13.4±0.7	14.6±0.7	17.4±0.5	17.2±0.5	18.1±0.3

Tab. 1 The irradiation parameters include the targeted and average measured temperatures as well as the damage doses.

The microstructural examinations were performed using the transmission electron microscope (TEM) Tecnai-F20 (product of the ThermoFisher Scientific Company), which is installed in the Fusion Materials Laboratory (hot cells) of the Karlsruhe Institute of Technology. The microscope is also equipped with a high-angle annular dark field detector (HAADF) with the possibility of scanning TEM (STEM).

The specimens for TEM analysis were prepared from undeformed parts of impact tests samples by cutting 0.3-0.4 mm thin plates and electrochemically etching at room temperature with a

Tenupol-3 jet polisher using a 20% H_2SO_4 + 80% CH_3OH solution. After the formation of a small hole, discs with 1 mm diameter were punched from the area around the hole. A special double tilt holder for 1mm discs was used for TEM analysis. The reduction of the sample size was necessary to minimize the radiation exposure during handling. The best imaging results were typically obtained in areas of 70-120 nm thickness, which was measured by electron energy loss spectroscopy (EELS). The uncertainty of 10% in thickness measurement is not significant compared to a 25% statistical error.

2.2. Analysis of dislocation loops

The microstructure of EUROFER97 visible in TEM is characterized by the martensite laths, which typically have a width of 200-400 nm and a variable length (0.5-3 μm) [14]. The laths represent smallest single crystal areas, which can be imaged with defined ***g***-conditions. The targeted orientation to achieve defined ***g***-conditions for such small grains in magnetic samples required a considerable experimental effort and was performed for only a few laths for each irradiation temperature. In order to improve the statistics, other data collection methods were also used. In the discussion section we present a comparison of the results obtained by applying different methods.

Dislocation loops formed in bcc materials by neutron irradiation show either $\boldsymbol{b}\langle 100\rangle$ or $\boldsymbol{b}\tfrac{1}{2}\langle 111\rangle$ Burgers vectors, which can be identified by different methods depending on the loop size. However, the most reliable but also the most time-consuming method is imaging of dislocation loops with four low-indexed ***g***-vectors near the [100] zone axis. The invisibility criteria for corresponding ***g***-vectors are shown in Tab. 2. This allows the identification of all $\boldsymbol{b}\tfrac{1}{2}\langle 111\rangle$ loops and 2/3 of the $\boldsymbol{b}\langle 100\rangle$ loops in the four images. Only the loops with $\boldsymbol{b}[100]$ Burges vector are

g \ ***b***	½[111]	½[$\bar{1}$11]	½[1$\bar{1}$1]	½[11$\bar{1}$]	[001]	[010]	[100]
[0$\bar{1}\bar{1}$]	**1**	**1**	**0**	**0**	**1**	**1**	0
[0$\bar{1}$1]	**0**	**0**	**1**	**1**	**1**	**1**	0
[020]	**1**	**1**	**1**	**1**	**0**	**2**	0
[002]	**1**	**1**	**1**	**1**	**2**	**0**	0

Tab. 2 $|\boldsymbol{g}\bullet\boldsymbol{b}|$ values for four possible ***g*** vectors near [100] ZA.

invisible in all four orientations. In the past, this analysis method has been already successfully applied for loops produced by neutron as well as by ion irradiation [15–18]. Carrying out ***g*** analysis near other zone axes is connected with an even higher uncertainty in Burgers vector determination.

The loops with different Burgers vectors can also be identified based on their projections on the viewing screen. The ***b***½⟨111⟩ loops show an oval projection whereas the on-edge view for ***b***⟨100⟩ loops shows the typical double-bean contrast near [100] ZA [16]. This method is suitable for loops larger than about 10 nm.

The statistical method can be used for the analysis of small loops or "black dots" with a high number density [19]. In such dot-structures it is almost impossible to trace individual loops in different ***g***-images. The disadvantage of this method is a relatively high statistical error of about 18%. Here and in the following we use the term "black dot" to indicate loops with a size typically smaller than 5 nm, so that the circular structure cannot be resolved.

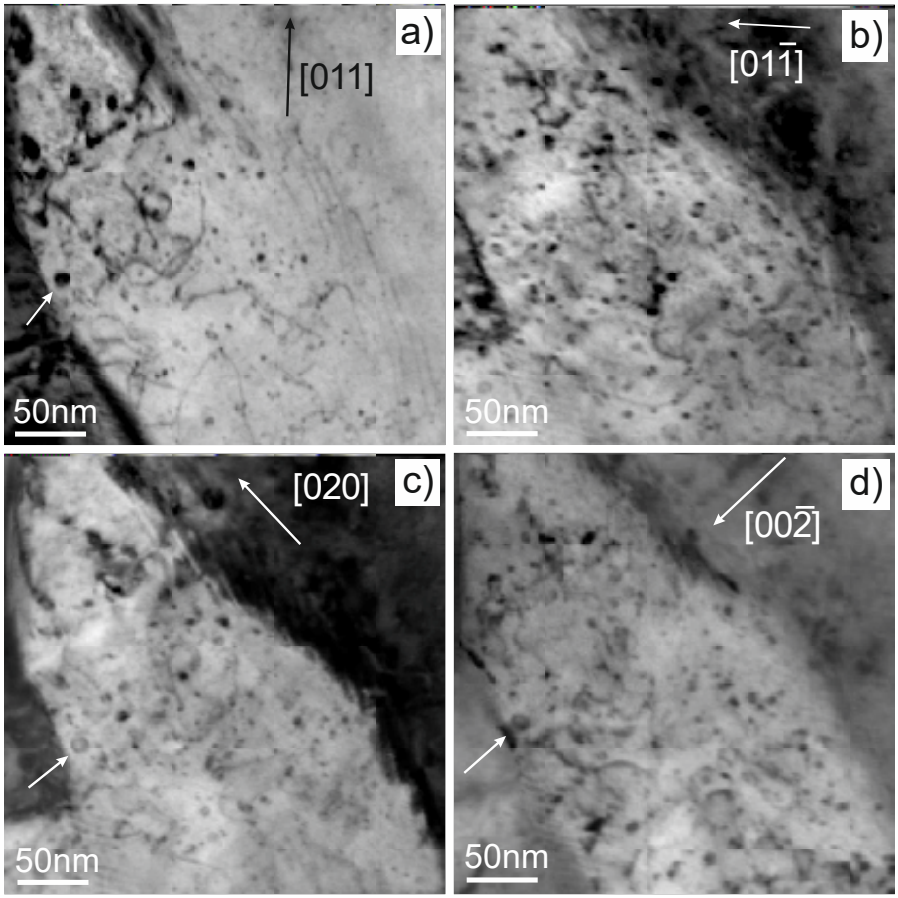

Fig. 1 DF TEM images with reverse contrast of material irradiated at 250°C. The images were obtained using different reflections g=[011], [01-1], [020] and [002] as labeled in the figures.

3. Results

3.1. Microstructural analysis of irradiated material

The results of ***g***-analysis near the [100] ZA for all irradiation temperatures are illustrated in Figs. 1-6. Figure 7 shows the corresponding size distribution histograms.

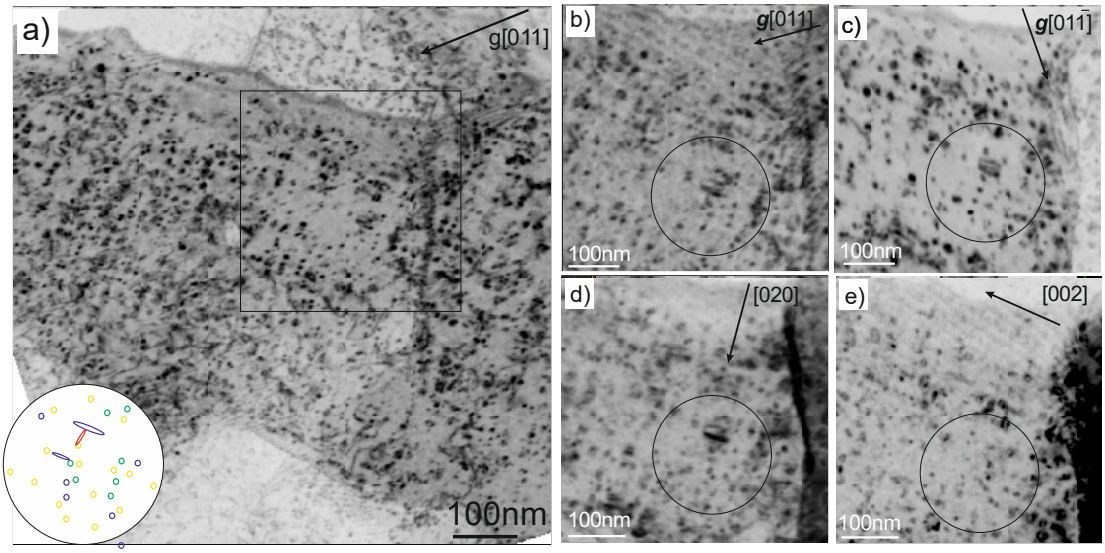

Fig. 2 DF TEM images with reverse contrast of material irradiated at 300°C. The image in part (a) shows the ordered dislocation loops in the investigated lath. The images in parts (b-e) show ***g***-analysis of the part marked by square. They were obtained using **g**=[011], [01-1], [020] and [002] reflections. The circular cropping in part (a) shows the analysis of defects in the area marked with a circle. The ***b***⟨100⟩ loops are schematically drawn with red and blue and ***b***½⟨111⟩ loops with yellow and green colors.

In the materials irradiated at 250°C and 300°C, radiation-induced defects have a size of less than 15nm (Figs. 1, 2 and Fig. 7a,b). Since EUROFER97 has a martensite structure, the monocrystalline regions with defined ***g***-conditions are laths with a size in the range of several hundred nanometers. The upper part of the analyzed lath in Fig. 1, which shows material irradiated at 250°C, has a misorientation of about ~3° to lower parts. For Fig. 1b,c, it was necessary to obtain TEM micrographs with the same **g**-conditions for both parts separately and composed them artificially. The majority of defects (~90%) are featureless "black dots" with Burgers vectors of the ***b***½⟨111⟩ type. A circular loop structure could be clearly recognized for only 12 defects out of 148 counted in the image. Their Burgers vectors are also of the ***b***½⟨111⟩ type as they have oval projections and are visible in two **g**⟨200⟩ images (Fig. 1c,d). For 300°C, the fraction of defects with circular structure increases to ~25%, whereas the rest of the defects is visible as "black dots" (Fig. 2). 80% of the larger "circular" loops and only 10% of the black dots show a Burgers vector of ***b***⟨100⟩ type. The "circular" ***b***⟨100⟩ loops appear "edge-on" and

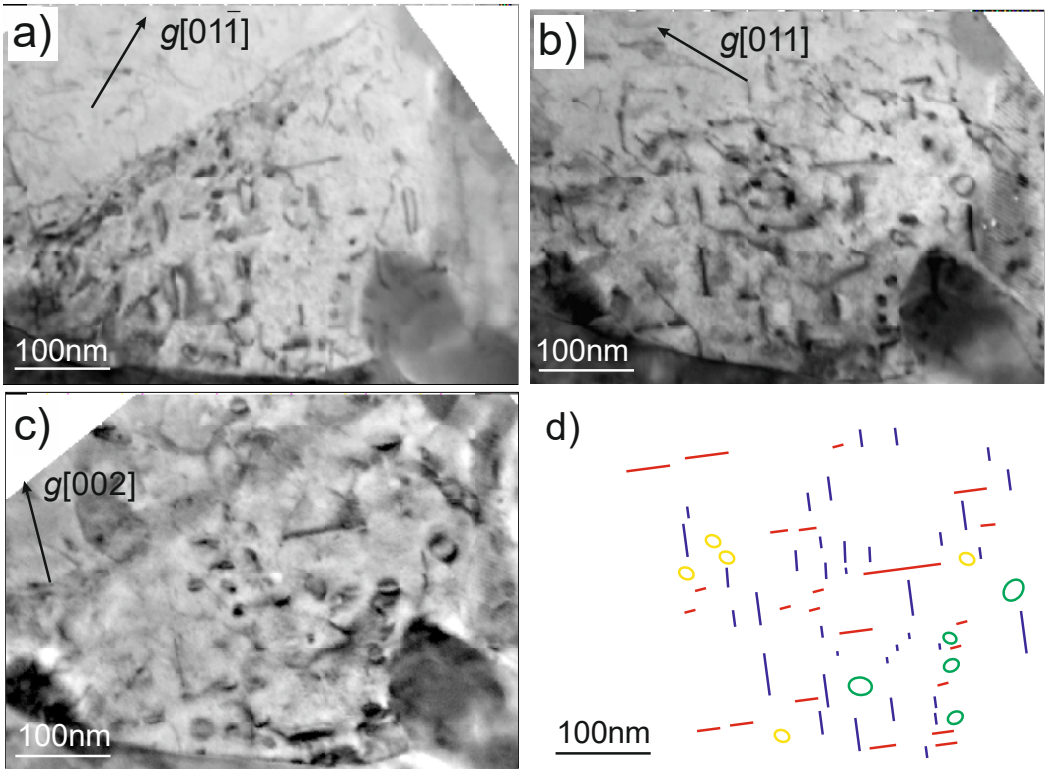

Fig. 3 DF TEM images with reverse contrast of material irradiated at 350°C. The images were obtained using different reflections g=[011], [01-1] and [002] as labeled in the figures. The ***b***⟨100⟩ loops are schematically drawn with red and blue and ***b***½⟨111⟩ loops with yellow and green colors in part (d).

parallel either to [001] or [010] directions.

The defects in the material irradiated at 300°C show a tendency to the spatial order along ⟨100⟩ directions (Fig. 2). The rectangular pattern of ordered dislocation loops is well visible in the images with moderate magnify

cation (Fig. 2a). The loops in the lines have both ***b***⟨100⟩ and ***b***½⟨111⟩ Burgers vectors. The loops with ***b***[010] are most probably present in [010] lines, whereas the ***b***[001] loops appear in the lines along [001] direction. The four ***g***-images in Fig. 2b-e show the analysis of Burgers vectors in the area marked with a square in Fig. 2a. The fraction of defects with circular structure increases to ~25%, whereas the rest of them is visible as black dots. The analysis of Burgers vector in the image section marked with circle is shown in the cutout (Fig. 2a). The black dots and loops are imaged with different colors depended on their Burgers vectors. The 7 loops ordered along [011] direction show a ***b***½⟨111⟩ Burgers vector and only one a ***b***⟨100⟩ Burgers vector. The analysis shows that 80% of "circular" loops and only 10% of black dots show a Burgers vector of the ⟨100⟩ type.

The material irradiated at 350°C contains a structure of dislocation loops and voids

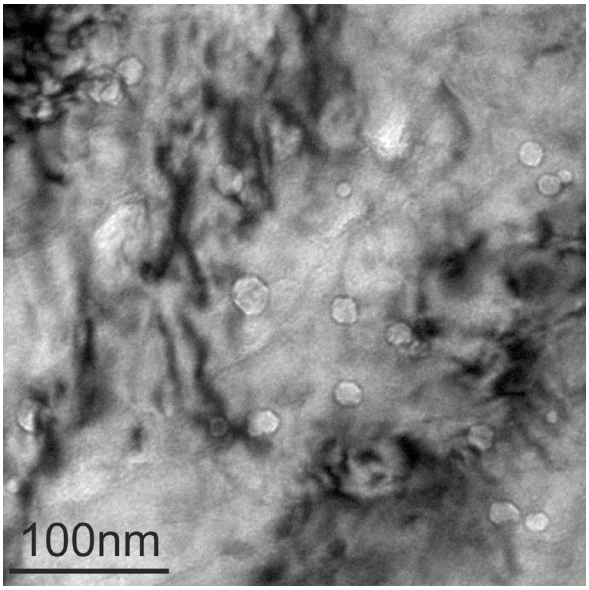

Fig. 4 Bright-field TEM micrograph: voids in material irradiated at 350°C.

(Fig. 3, 4). About 90% of the loops show a $\boldsymbol{b}\langle 100\rangle$ Burgers vector, whereas a small fraction with size less than 25nm have $\boldsymbol{b}\frac{1}{2}\langle 111\rangle$. The $\boldsymbol{b}\frac{1}{2}\langle 111\rangle$ loops are visible with inclined oval projection and imaged with yellow and green colors in the schematic drawing of dislocation loops (Fig. 3d). The voids formed at this temperature show a size less than 25nm (Fig. 4). They are inhomogeneously distributed in the material and cause the estimated void swelling of 0.18%.

The dislocation loops of both types were also found in the specimens irradiated at 400°C and 415°C (Fig. 5, 6). The dislocation loops have sizes in the range of 70-200nm. Additionally, voids of a very low number

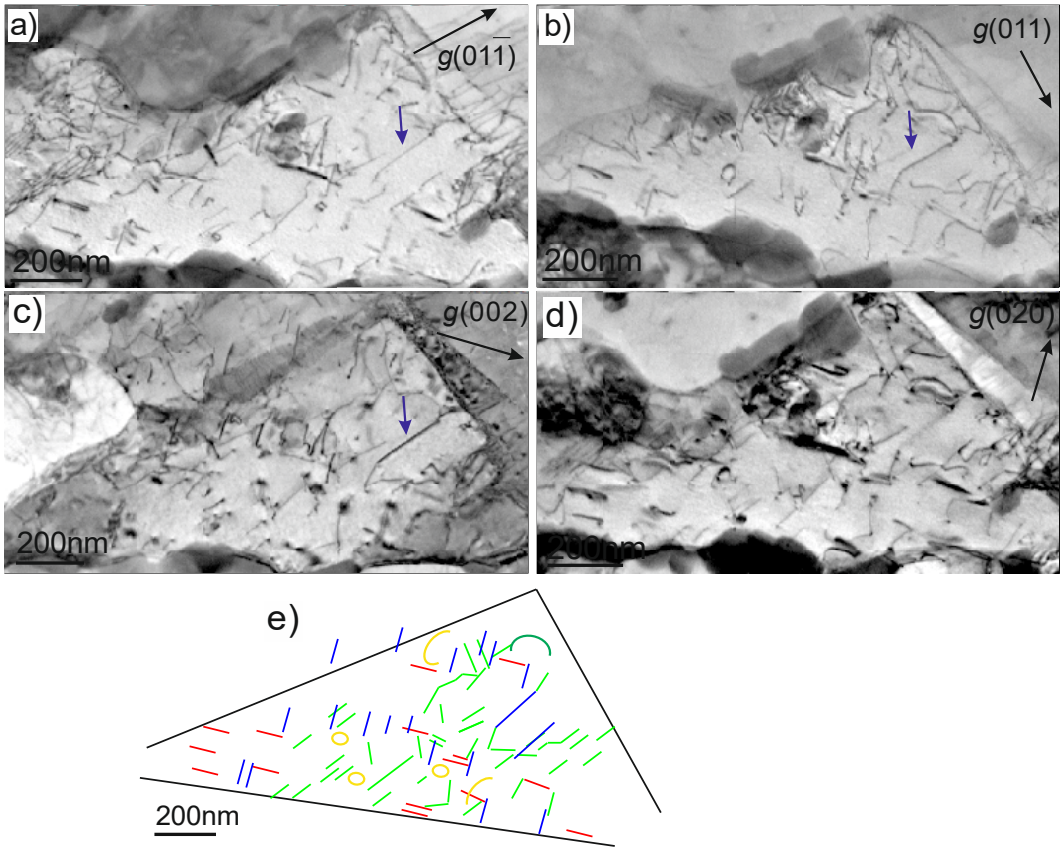

Fig. 5 DF TEM images with reverse contrast of material irradiated at 400°C. The images in parts (a-b) were obtained using different reflections $\boldsymbol{g}$=[011], [01-1], [020] and [002] as labeled in the figures. The $\boldsymbol{b}\langle 100\rangle$ loops are schematically drawn with red and blue and $\boldsymbol{b}\frac{1}{2}\langle 111\rangle$ loops with yellow and green colors in part (e).

density were found in the specimen irradiated at 400°C. The significant part of dislocation loops at these temperatures is of the same order of magnitude as the specimen thickness of ~70-120nm. The large loops are often cut by the TEM foil surface and are seen in the images as curved line dislocations. Their identification and differentiation from the numerous line dislocations are possible only after detailed ***g***-analysis. In the unirradiated EUROFER97 no ***b***⟨100⟩ line dislocations were found. Therefore, we suggest that all ***b***⟨100⟩ curved dislocations are part of the larger ***b***⟨100⟩ loops. Their real size can then be estimated based on the curvature. Especially this problem concerns the analysis of the loops in the material irradiated at 415°C. A detailed analysis of an area with two ***b***⟨100⟩ loops (marked by arrows) is shown in Fig. 6. Their size was estimated to be in the range of 150-180nm. The loops are not really distinguishable from the normal line dislocations in only one ***g***-image.

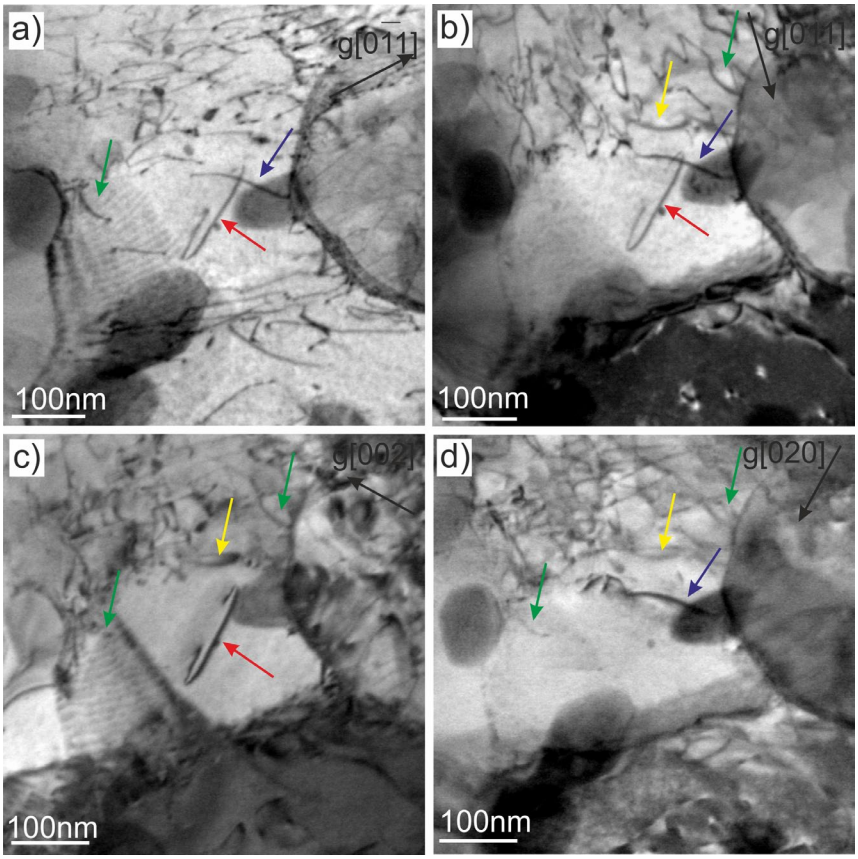

Fig. 6. DF TEM images with reverse contrast of material irradiated at 450°C. The images were obtained using different reflections g=[011], [01-1], [020] and [002] as labeled in the figures. The ***b***⟨100⟩ loops are marked with red and blue and ***b***½⟨111⟩ loops with yellow and green arrows.

We also found several "curved lines" with ***b***½⟨111⟩ which could also be identified as cut-off sections of dislocation loops. Two of them are marked with yellow and green arrows in Fig. 6. In contrast to the standard line screw dislocations where the Burgers vector is parallel

to the dislocation line, these appear as edge dislocations where the Burgers vector is perpendicular to the dislocation line. This is consistent with the assumption that the “curved lines” $\boldsymbol{b}$½⟨111⟩ are part of the dislocation loops. It should be mentioned that not all such loops can be clearly recognized among line dislocations, therefore, the number density of radiation-induced defects could be significantly higher than the given measured values.

4. Discussion

4.1. Quantitative analysis of radiation-induced defects

The size distribution histograms of the dislocation loops are displayed in different colours in Fig 7. Most loops formed at 250°C and 300°C are highly disperse "black dots" of a few nanometers (Fig. 7a). At temperatures ≤300°C the majority of defects are "black dots" with sizes typically less than 5nm (Figs. 1, 2). Their quantity reaches 90% at 250°C and 70% at 300°C. By "black dots" we mean small dislocation loops (≤6 nm size), which are spot (dot) like images with no recognizable structure in the TEM analyses. On the other hand, the larger loops typically show a circular structure. In general, the size at which the loops will appear as rings depends strongly on the sample thickness, alignment of the $\boldsymbol{g}$-vector, application of weak beam orientation and other imaging conditions. The dividing line at 7 nm in the diagram (Fig. 7a) shows the boundary between black points and circular loops. At higher radiation temperatures the loop size increases strongly and reaches ~180 nm at 415°C (Fig. 7b). The size distribution for 415°C was drawn with the dashed line due to the poor statistics and significant

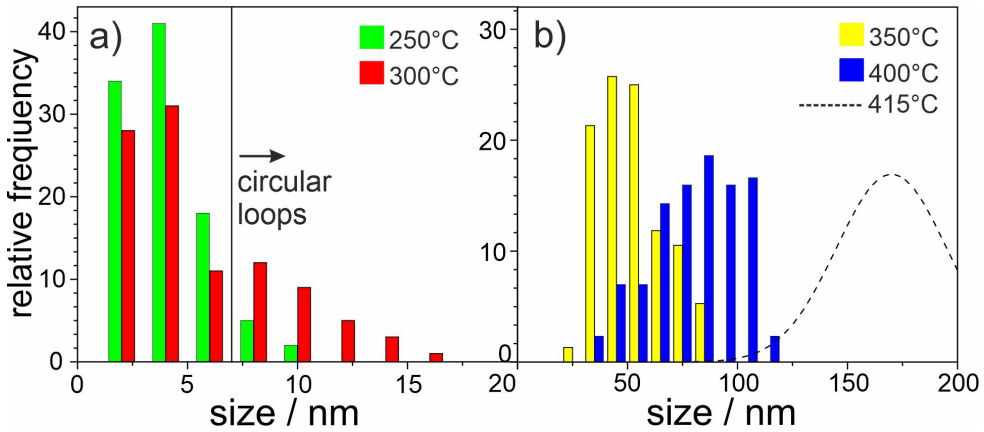

Fig. 7 Size distribution histograms of dislocation loops for 250°C and 300°C as well as for 350°C and 400°C irradiation temperatures (a,b). The estimated size distribution for 450°C was plotted as a dashed line in the part (b) due to the lack of reliable statistics.

uncertainties in the size estimation. Loops larger than 100 nm are in most cases not fully preserved in the TEM foil and their actual size has been estimated. The large loops can be identified as such, if at least 1/3 of the original circle remains in the thin foil, so that a considerable proportion of the smaller sections of the loops has been excluded from the statistics. This also influences the results of the size evaluation of the sample irradiated at 400°C.The drawing of a histogram for 415°C has been omitted because of poor statistics and considerable uncertainties in size estimation. Moreover, the cut section of the loop can be recognized as such if it has at least 1/3 of the original circle, so a notable fraction of the smaller loops sections was not recognized as a "radiation-induced defect".

The average loop size and the number density as a function of the irradiation temperature are shown in Fig. 8a,b (red squares). The size increases from less than 10 nm in the material irradiated at ≤300°C to 180 nm at 415°C (Fig. 8a). The number densities of visible dislocation loops are drawn in Fig. 8b as a logarithmic function for all irradiation temperatures (red squares). The highest number density of dislocation loops $4.6 \cdot 10^{22}$ m^{-3} was measured at 300°C,

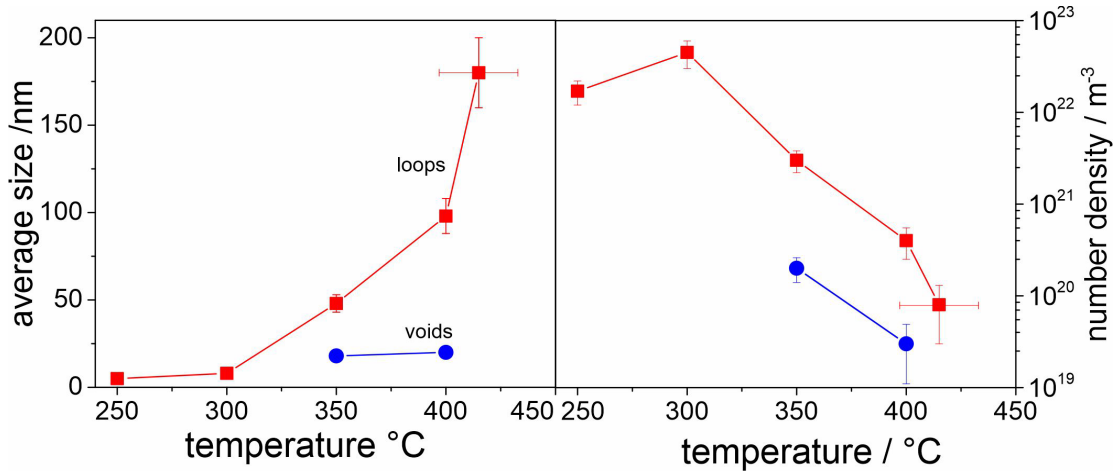

Fig. 8 Dependence of average size of dislocation loops and voids (blue circles) on irradiation temperature (a) and number density (b).

whereas at 250°C it amounted to $1.6 \cdot 10^{22}$ m^{-3}. The value decreases continuously toward 415°C irradiation temperature, resulting in a value more than two orders of magnitude lower compared to that at 250°C.The voids were detected only in the material irradiated at 350°C and 400°C (blue circles in Fig. 8a,b). Their average size is about 18 nm at 350°C and 20 nm at 400°C. At 400°C, the voids show a very low number density. The swelling and density numbers were estimated with an error of 70%.

The displacement of atoms caused by neutron irradiation generates both, interstitials and vacancies, which merge into dislocation loops with interstitial character and voids. The voids

are formed by clustering a small part of the vacancies in the intermediate temperature range ≈0.3-0.6T_m. In EUROFER97, the formation of voids was observed only at 350°C and 400°C with 0.2% and 0.04% cavity swelling, respectively (Fig. 9). The swelling caused by the presence of voids is usually calculated as a simple sum of the volumes of all voids observed, divided by the volume of the material in which the cavities were counted [20].

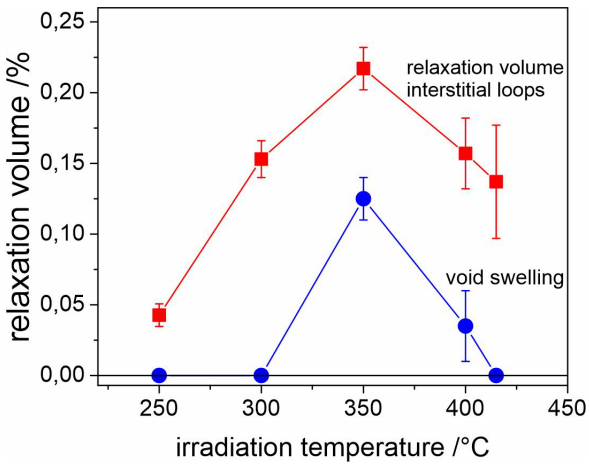

Fig. 9 Relaxation volume caused by dislocation loops (red squares) and void swelling (blue squares) as a function of radiation temperature.

The interstitial defects support the formation and growth of interstitial loops during irradiation because the large elastic misfit associated with an interstitial defect causes dislocations to attract interstitials more strongly than vacancies [21]. Such formation of additional circular plates, i.e. interstitial loops, causes significant swelling in single crystals [22]. The diagram in Fig. 9 shows relaxation volumes (red squares) and void swelling (blue circles) for all irradiation temperatures. The both values reached a maximum at 350°C. For comparison, the number density reaches its maximum at 300°C (Fig. 8b). At the temperatures ≥400°C the measuring error increases significantly, since the loop size could not be determined exactly in all cases.

The maximum of the relaxation volume of 0.21% was reached at the irradiation temperature of 350°C. At this temperature the void swelling also shows the highest value of 0.13%. The previous investigations show that the radiation-induced void swelling reaches the maximum value at 420°C [23]. It was also assumed that no void and loops were formed at the higher temperatures. Our results confirm these conclusions only in relation to voids which were detected at higher temperature in materials with higher helium concentration [24]. On the other hand, we clearly show that the formation of loops also occurred at higher temperatures, but they are not always visible in the TEM (Fig. 6). It should also be mentioned that the maximum of void swelling appears in EUROFER97 at ~50°C lower temperature than in F82H steel [23]. The formation of loops with the size >150nm in pure single crystal iron after ion irradiation at 500°C was reported in [25]. The absence of a grain boundary or other inhomogeneities can lead to the formation of loops with a size of several hundred nanometers. In the present study, the

lath size is in the range of 300-400nm, so that the majority of the loops touch the lath boundaries. This finally leads to transforming them into common line dislocations increasing their density.

Tab. 3 summarizes all relevant statistical and quantitative data on dislocation loops and voids extracted by analyzing, among others, the presented TEM images. The data includes average size, number density, Burgers vector, fraction of $\boldsymbol{b}$½⟨111⟩ loops, swelling and relaxation volume. The average size of dislocation loops was obtained by counting several hundred loops in the specimens irradiated at 250°C and 300°C. For 350°C and 400°, the statistical data was obtained from up to 150 single loops, whereas for 415°C, only 27 loops were counted. The total number density of radiation-induced defects was obtained taking into account that part of the defects is invisible at defined $\boldsymbol{g}$-conditions. In the images with $\boldsymbol{g}$⟨200⟩, 100% of $\boldsymbol{b}$½⟨111⟩ loops and only 1/3 of $\boldsymbol{b}$⟨100⟩ loops are visible. Correspondingly, ½ of $\boldsymbol{b}$½⟨111⟩ loops and 2/3 of $\boldsymbol{b}$⟨001⟩ loops

T_{irr}	total number of loops	loop number density /$\times 10^{20}$ m^{-3}	average size /nm	void number density /$\times 10^{20}$ m^{-3}	void swelling %	relaxation volume /%	fraction of ½⟨111⟩ loops
250°C	367	150±40	5	---------	-------	0.024±0.01	90%
300°C	460	460±120	7	---------	------	0.087±0.03	73%
350°C	157	45±6	48	3.2±0.8	0.12	0.215±0.07	21%
400°C	134	2.5±1.2	105	0.035±0.015	0.02	0.155±0.08	13%
450°C	27	0.75±0.25	180	---------	-------	0.145±0.10	20%

Tab. 3 Summary of quantitative parameters and statistical data of “black dots”, dislocation loops and voids.

are visible in the images with $\boldsymbol{g}$⟨011⟩. The average from different $\boldsymbol{g}$-images of several lathes was taken as the total number density value of the dislocation loops.

4.2. Burgers vectors of dislocation loops

The experiments have identified formation of two kinds of dislocation loops with $\boldsymbol{b}$½⟨111⟩ and $\boldsymbol{b}$⟨100⟩ Burgers vectors at all irradiation temperatures. The fraction of the $\boldsymbol{b}$½⟨111⟩ loops changes with the irradiation temperature as is shown in the bar diagram in Fig. 10 and listed in Tab.3.

As shown in the diagram, 95% of all analyzed defects at 250°C and 73% at 300°C show Burgers vectors of $\boldsymbol{b}$½⟨111⟩ type (Fig. 10). These are mainly the "black dots", of which about 90% at 250°C and 80% at 300°C show $\boldsymbol{b}$½⟨111⟩ Burgers vector. For the larger circular loops, the fraction with $\boldsymbol{b}$½⟨111⟩ Burgers vector decreases to 75% for 250°C to 20% for 300°C.

The Burgers vectors of ~20% of "black dots" could not be clearly identified due to the overlapping in different $\boldsymbol{g}$-images. These undefined defects were excluded from the Burgers vector statistics, but were taken into account when calculating the number density. These results were verified by a statistical analysis including the calculation of total number densities based on the visible number densities for individual $\boldsymbol{g}$-images [19]. It was found that the statistical method systematically yields 15-20% lower values for $\boldsymbol{b}$½⟨111⟩ loops fraction compared to the direct visibility method. The error of this method, which is specified for the analysis of an undeformed monocrystalline area, is given as 18%. [19]. It can be expected that the statistical error for analysis of martensite materials with a lath structure can be up to 25%. The reasons for this are residual contrasts in $\boldsymbol{g}$-images caused by the slight deformation of the thin film in the strong magnetic field of the objective lens inside the TEM. The defined $\boldsymbol{g}$-conditions $|\boldsymbol{b}\bullet\boldsymbol{g}|=0$ or $|\boldsymbol{b}\bullet\boldsymbol{g}|=1,2$ can then only be applied to a small part of the observed area. This strongly influences the visibility of small defects and leads to the distortions in the statistics. This applies in particular to the $\boldsymbol{g}$[020] and $\boldsymbol{g}$[002] images, where $\boldsymbol{b}$½⟨111⟩ "black dots have a lower value $|\boldsymbol{b}\bullet\boldsymbol{g}|=1$ than the $\boldsymbol{b}$[010] (or $\boldsymbol{b}$[001]) defects with $|\boldsymbol{b}\bullet\boldsymbol{g}|=2$ and thus weaker contrasts (Tab. 2). The results of the statistical analysis are then systematically shifted to a larger proportion of $\boldsymbol{b}$⟨100⟩ loops. For these reasons, we assume that standard analyses should be more reliable than statistical evaluation. The statistical method was omitted at the higher irradiation temperatures, since the individual loops are clearly visible in all $\boldsymbol{g}$-images.

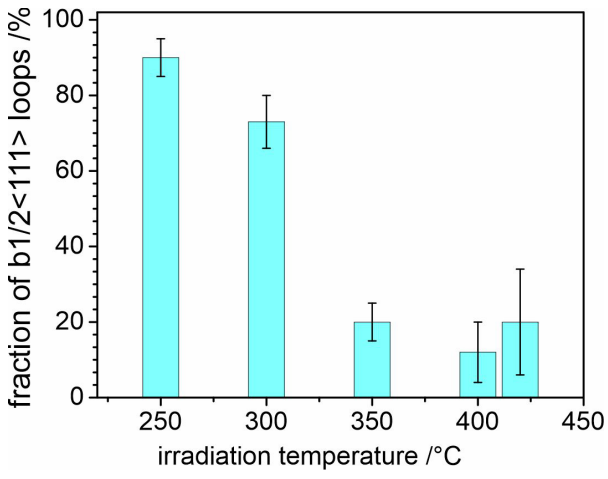

Fig. 10 Fraction of $\boldsymbol{b}$½⟨111⟩ dislocation loops as a function of radiation temperature.

At irradiation temperatures above 350°C, $\boldsymbol{b}$⟨100⟩ loops became more dominant than $\boldsymbol{b}$½⟨111⟩ loops which fraction reduces to 20% (Fig. 9). At temperatures ≥400°C the fraction of $\boldsymbol{b}$½⟨111⟩ loops is

less than 20%. The evaluation was performed by the above-mentioned examination of visibility under defined ***g***-conditions (Tab. 2) and by checking the loops' projection on the image plane as described in [16]. Both methods show the same result, but the latter was preferably used to improve statistics due to the lower experimental effort.

The diameter of the dislocation loops in the material irradiated at 400°C or 415°C is often larger than the thickness of the TEM foil, and the loops are visible only as parts of the circle or as bows. Such bows are not clearly distinguishable from the typical curved ***b***½⟨111⟩ line dislocations in the unirradiated EUROFER97. The Burgers vector analysis shows that several "bows" are edge dislocations with ***b***⟨100⟩ Burgers vector. It is also known that such dislocations are not present in the unirradiated EUROFER97. Accordingly, all detected ***b***⟨100⟩ "bows" were assigned to the loops formed by neutron irradiation. Two such loops are marked in Fig. 6 with red and blue arrows. Their size was estimated from the curvature. In almost all cases, the ***b***⟨100⟩ loops have a {100} habit plane, however, in Fig. 4, we see a ***b***⟨100⟩ dislocation with the line oriented in [111] direction (blue line in part (e)). It can be assumed that this is a junction of two larger ***b***½⟨111⟩ loops. These dislocations were not included in the statistics.

Since the line dislocation are present in unirradiated EUROFER97, a distinction between them and ***b***½⟨111⟩ large loops is not possible with certainty. Analyzing of various ***g***-images it was found that, several ***b***½⟨111⟩ edge bow-shaped dislocations loops as radiation induced loops. In Fig 6, such bows are marked yellow arrows. We have also assigned all detected ***b***½⟨111⟩ edge dislocations with curved shape as part of the ***b***½⟨111⟩ loops. This analysis does not claim to be complete, as the identification of special curvature within a network of line dislocations is not reliably possible. It can be assumed that at 400°C and 415°C, the proportion of ***b***½⟨111⟩ loops is even higher than estimated.

A comparison of our results with the literature is rather difficult, since all neutron irradiation campaigns clearly differ from each other in material, dose and irradiation temperature. A good overviews about microstructure of neutron irradiated ferritic steels is shown in [13]. The strong influence of the subjective factor on the identification and quantitative analysis of dislocation loops and especially of "black dots" has recently been under discussion. Parameters of dislocation loops can be influenced by many factors, such as the presence of He, Cr concentration or presence of other alloying elements. There is a tendency for the ***b***½⟨111⟩ loops to dominate at ≤300°C radiation temperatures, while the ***b***⟨100⟩ loops are often much more common at temperatures of ≥350°C. Similar variations of the ***b***½⟨111⟩ fraction with radiation

temperature in the 300°C-500°C range were observed in ion irradiated pure Fe [25]. While at 300°C only the $\boldsymbol{b}$½⟨111⟩ loops were detected, at 500°C exclusively the $\boldsymbol{b}$⟨100⟩ loops could be seen.

As claimed in earlier publications, there are major differences in the interpretation of microstructural results where the reported proportion of $\boldsymbol{b}$½⟨111⟩ loops varies widely. In our opinion, the main reason for this is the subjective criteria for the visibility of the small defect ("black dots") [26]. Whether the loops are identified as such depends largely on the observer the contrast of interstitial defects of a few nanometers is very sensitive to the alignment of $\boldsymbol{g}$-vectors, the thickness of the TEM foil and the local deformation or bending. Also, the identification of large dislocation loops of $\boldsymbol{b}$⟨100⟩ type occurring at higher temperatures is not clearly described. The loops with several hundred nanometers were well identified in the single crystal material [25], but cannot be clearly distinguished from the typical line dislocation in structural materials with the martensite laths. Also, the identification of large dislocation loops of that occur at higher temperatures is not clearly described. The loops with several hundred nanometers were well identified in the large grains which were without dislocations before irradiation [25], but in the thin lathes they are not clearly distinguishable from the typical line dislocation.

4.3. Effect of radiation induced defects on mechanical properties

Previous studies show a noticeable influence of neutron irradiation on the tensile properties of different RAFM alloys [6,18,27]. The displacement of atoms caused by neutron irradiation generates both interstitials and vacancies, which merge into dislocation loops with interstitial character and cavities. The interstitial defects support the formation and growth of interstitial loops during irradiation because the large elastic misfit associated with an interstitial defect causes dislocations to attract interstitials more strongly than vacancies [21]. The migration of less mobile vacancies leads to the formation of voids in the narrow temperature range 330°C-450°C [20,23].

The origin of radiation-induced hardening generally stems from the formation of various types of radiation-induced defects. The interaction between a line dislocation and an irradiation-induced defect strongly influences the dislocation movement and significantly affects the yield strength of the material. Similarly, the oxide nanoclusters in ODS and the irradiation-induced

phases in ferritic-martensitic alloys also serve as dislocation pinning that contribute to hardening and increase the yield strength of the alloy.

Dispersed barrier hardening (DBH), Friedel Kroupa Hirsch (FKH) and Bacon Kocks Scattergood (BKS) models are often used to predict hardening caused by radiation induced defects such as voids or dislocation loops [18,27–29]. The FKH model was originally developed for loop hardening in *fcc* metals and also provides a good fit for the hardening in *bcc* metals when multiplied by a single parameter α_{FKH} for the loops size <10nm [28]. In the present case, this model can only be used for the hardening calculation at 250°C and 300°C where loops with a size of <10nm have been detected. The BKS model was shown to accurately predict hardening for the voids [28]. Since irradiated EUROFER97 has voids and dislocation loops with wide size variation, the DBH model is more favorable to describe the relationship between microstructure and radiation-induced hardening ($\Delta\sigma_y$), taking into account the individual obstacle strength factor **α** [18,27,29]:

$$\Delta\sigma_y = M\alpha\mu b\sqrt{n_x d} \qquad (1)$$

where ***M*** is the Taylor factor (3.06 for bcc steels), ***μ*** the shear modulus of the matrix which was taken 78 GPa for 250°C and 68 GPa for 415°C [30], ***b*** the magnitude of the Burgers vector of the moving dislocation (0.249nm) and **α** the obstacle strength factor takes value 0<α<1 [31].

T_{irr}	Burgers vector	$\mathbf{n_x}$ /•10^{20} m^{-3}	average size **d** /nm	strengthening σ_y /MPa	Total strengthening **σ** /MPa
250°C	***b***½⟨111⟩	150±35	5	77	**96**
	b½⟨100⟩	15±5	5	54	
300°C	***b***½⟨111⟩	340±60	6	130	**213**
	b½⟨100⟩	120±30	8	169	
350°C	***b***½⟨111⟩	9.5±2.5	20	42	**251**
	b½⟨100⟩	37.2±5	48	220	
	voids	3.2±0.8	18	111	
400°C	***b***½⟨111⟩	0.25±0.10	25	7	**93**
	b½⟨100⟩	2.25±0.5	110	77	
	voids	0.03±0.02	20	14	
415°C	***b***½⟨111⟩	0.10±0.05	100	11	**54**
	b½⟨100⟩	0.70±0.25	180	52	

Tab. 4 Calculation of radiation induced strengthening based on obstacle strengthening model.

The values of number density $\mathbf{n_x}$ and average size **d** of radiation induced defects was measured from TEM analysis (Tab. 4).

TEM observation show the presence of three types of radiation induced obstacles: the ***b***½⟨111⟩, ***b***½⟨100⟩ loops and voids. The model proposed by Field et al.[18] shows that the total hardening can be calculated as root sum square superposition with barrier strength factor α=0.17 for ***b***½⟨111⟩ and α=0.33 for ***b***⟨100⟩ loops [18]. The strength factor α=1 was taken for voids with size >10nm [27]. The densities and sizes of all these defects were calculated separately for each radiation temperature.

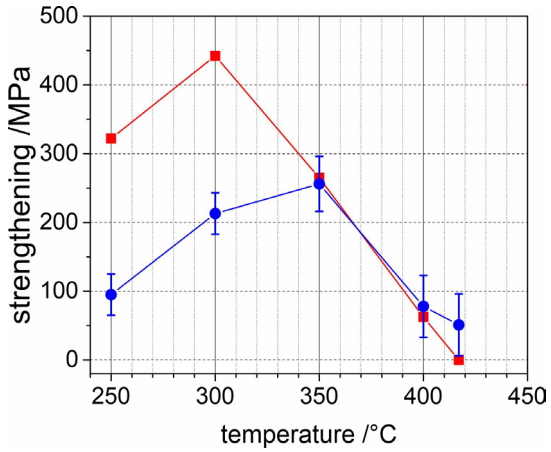

Fig. 11 Radiation induced hardening measured by tensile tests (red squares) and calculated based on DBH model (blue squares).

The comparison of measured (red squares) [6] and calculated (blue squares) strengthening as a function of the radiation temperature is shown in Fig. 11. The measured strengthening shows a considerable increase at 300°C [6] indicates an effective pinning of dislocation lines at the radiation induced defects. At high temperatures the strengthening decreases continuously and at 415°C reaches approximately the same value as unirradiated EUROFER97. The effect of other defects such as grain or lattice boundaries and precipitates plays a more significant role in pinning of dislocation lines at higher temperatures. For the temperatures ≥350°C, the model and experimental data show a good correlation. At irradiation temperatures of 250°C and 300°C, the calculated strengthening is lower by 150-200 MPa compared to experiment. The application of the FKH model does not lead to any essential changes in the result.

The substantial difference between model and experiment at lower temperatures suggest the presence of defects which are not visible in TEM. Several SANS studies confirm the presence of small (<3nm) nano-voids in EUROFER97 at 250°C [32,33]. The voids have a high number density and certainly increase hardening despite their low barrier strength. At 350°C the increased diffusion of vacancies allows the formation of voids with a sizes up to 30nm, which are clearly visible in TEM images. At these and higher temperatures, the hardening calculated from the distribution of the radiation-induced defects observed by TEM corresponds to the experimentally measured value.

5. Summary

The defects generated by neutron irradiation at different temperatures in EUROFER97 were the subject of a comprehensive TEM study. The microstructure of material irradiated at the temperature lower than 300°C is dominated by small dislocation loops and black dots mainly of the b½⟨111⟩ type. Neutron irradiation at higher temperatures leads to the formation of mainly b⟨100⟩ loops with a size of several tens of nanometers. The dislocation loops at 400°C and 415°C are particularly larger than the foil thickness. They are then often visible as bows, what makes their reliable identification more difficult and leads to a larger error in the statistic. The formation of voids was detected only at 350°C and 400°C.

The maximum number density of dislocation loops of $4.5*10^{22}$ m^{-3} was measured for 300°C. While, as expected, it decreases by two orders of magnitude by increasing the irradiation temperature to 415°C, the decrease by a factor ~3 was also observed at a lower temperature of 250°C. The behavior correlates well with the temperature dependence of the yield strength, which also has a maximum at 300°C. However, the void swelling and relaxation volume of dislocation loops show maximum values at 350°C.

The DBH model was found to accurately predict the strengthening in the material irradiated at the temperatures ≥350°C. The difference between the experiment and the DBH model at lower temperatures is caused by the formation of nano-voids or interstitial loops with a size of <3nm, which have been detected by SANS experiments, but are not well visible in the TEM images.

Acknowledgment

This work has been carried out within the framework of the EUROfusion Consortium and has received funding from the Euratom research and training programme 2014-2018 and 2019-2020 under grant agreement No 633053. The views and opinions expressed herein do not necessarily reflect those of the European Commission.

Figure Captions

Fig. 1 DF TEM images with reverse contrast of material irradiated at 250°C. The images were obtained using different reflections g=[011], [01-1], [020] and [002] as labeled in the figures.

Fig. 2 DF TEM images with reverse contrast of material irradiated at 300°C. The image in part (a) shows the ordered dislocation loops in the investigated lath. The images in parts (b-e) show ***g***-analysis of the part marked by square. They were obtained using **g**=[011], [01-1], [020] and [002] reflections. The circular cropping in part (a) shows the analysis of defects in the area marked with a circle. The ***b***⟨100⟩ loops are schematically drawn with red and blue and ***b***½⟨111⟩ loops with yellow and green colors.

Fig. 3 DF TEM images with reverse contrast of material irradiated at 350°C. The images were obtained using different reflections g=[011], [01-1] and [002] as labeled in the figures. The ***b***⟨100⟩ loops are schematically drawn with red and blue and ***b***½⟨111⟩ loops with yellow and green colors in part (d).

Fig. 4 Bright-field TEM micrograph voids in material irradiated at 350°C.

Fig. 5 DF TEM images with reverse contrast of material irradiated at 400°C. The images in parts (a-b) were obtained using different reflections ***g***=[011], [01-1], [020] and [002] as labeled in the figures. The ***b***⟨100⟩ loops are schematically drawn with red and blue and ***b***½⟨111⟩ loops with yellow and green colors in part (e).

Fig. 6. DF TEM images with reverse contrast of material irradiated at 415°C. The images were obtained using different reflections g=[011], [01-1], [020] and [002] as labeled in the figures. The ***b***⟨100⟩ loops are marked with red and blue and ***b***½⟨111⟩ loops with yellow and green arrows.

Fig. 7 Size distribution histograms of dislocation loops for 250°C (green bars) and 300°C (red bars) in part (a) as well as 350°C (yellow bars) and 400°C (blue bars) in part (b). The size distribution for 415°C was plotted as a dashed line in (b) due to the lack of reliable statistics.

Fig. 8 Dependence of average size of dislocation loops (red squares) and voids (blue circles) on irradiation temperature (a) and number density (b).

Fig. 9 Relaxation volume caused by dislocation loops (red squares) and void swelling (blue squares) as a function of radiation temperature.

Fig. 10 Fraction of ***b***½⟨111⟩ dislocation loops as a function of radiation temperature.

Fig. 11 Radiation induced hardening measured by tensile tests (red squares) and calculated based on (DBH) model (blue squares).

References

[1] N. Baluc, D.S. Gelles, S. Jitsukawa, A. Kimura, R.L. Klueh, G.R. Odette, B. van der Schaaf, J. Yu, Status of reduced activation ferritic/martensitic steel development, Journal of Nuclear Materials 367-370 (2007) 33–41.

[2] F. Tavassoli, Eurofer Steel, Development to Full Code Qualification, Procedia Engineering 55 (2013) 300–308.

[3] A.-A.F. Tavassoli, A. Alamo, L. Bedel, L. Forest, J.-M. Gentzbittel, J.-W. Rensman, E. Diegele, R. Lindau, M. Schirra, R. Schmitt, H.C. Schneider, C. Petersen, A.-M. Lancha, P. Fernandez, G. Filacchioni, M.F. Maday, K. Mergia, N. Boukos, Baluc, P. Spätig, E. Alves, E. Lucon, Materials design data for reduced activation martensitic steel type EUROFER, Journal of Nuclear Materials 329-333 (2004) 257–262.

[4] R. Lindau, A. Möslang, M. Rieth, M. Klimiankou, E. Materna-Morris, A. Alamo, A.-A.F. Tavassoli, C. Cayron, A.-M. Lancha, P. Fernandez, N. Baluc, R. Schäublin, E. Diegele, G. Filacchioni, J.W. Rensman, B.v.d. Schaaf, E. Lucon, W. Dietz, Present development status of EUROFER and ODS-EUROFER for application in blanket concepts, Fusion Engineering and Design 75-79 (2005) 989–996.

[5] B. van der Schaaf, F. Tavassoli, C. Fazio, E. Rigal, E. Diegele, R. Lindau, G. LeMarois, The development of EUROFER reduced activation steel, Fusion Engineering and Design 69 (2003) 197–203.

[6] E. Materna-Morris, H.-C. Schneider, A. Möslang, Tensile behavior of RAFM alloys after neutron irradiation of up to 16.3 dpa between 250 and 450 °C, Journal of Nuclear Materials 455 (2014) 728–734.

[7] J. Aktaa, C. Petersen, Modeling the influence of high dose irradiation on the deformation and damage behavior of RAFM steels under low cycle fatigue conditions, Journal of Nuclear Materials 389 (2009) 432–435.

[8] C. Petersen, V. Shamardin, A. Fedoseev, G. Shimansky, V. Efimov, J. Rensman, The ARBOR irradiation project, Journal of Nuclear Materials 307-311 (2002) 1655–1659.

[9] M. Kytka, M. Brumovsky, M. Falcnik, Irradiation embrittlement characterization of the EUROFER 97 material, Journal of Nuclear Materials 409 (2011) 147–152.

[10] E. Gaganidze, B. Dafferner, H. Ries, R. Rolli, H.C. Schneider, J. Aktaa, Irradiation programme HFR phase IIb - SPICE. Impact testing on up to 16.3 dpa irradiated RAFM steels. Final report for task TW2-TTMS 001b-D05, Karlsruhe.

[11] E. Materna-Morris, A. Möslang, R. Rolli, H.-C. Schneider, Effect of helium on tensile properties and microstructure in 9%Cr–WVTa–steel after neutron irradiation up to 15dpa between 250 and 450°C, Journal of Nuclear Materials 386-388 (2009) 422–425.

[12] M. Klimenkov, E. Materna-Morris, A. Möslang, Characterization of radiation induced defects in EUROFER 97 after neutron irradiation, Journal of Nuclear Materials 417 (2011) 124–126.

[13] C. Dethloff, E. Gaganidze, J. Aktaa, Microstructural defects in EUROFER 97 after different neutron irradiation conditions, Nuclear Materials and Energy 9 (2016) 471–475.

[14] M. Klimenkov, R. Lindau, E. Materna-Morris, A. Möslang, TEM characterization of precipitates in EUROFER 97, Progress in Nuclear Energy 57 (2012) 8–13.

[15] M. Klimenkov, U. Jäntsch, M. Rieth, H.C. Schneider, D.E.J. Armstrong, J. Gibson, S.G. Roberts, Effect of neutron irradiation on the microstructure of tungsten, Nuclear Materials and Energy 9 (2016) 480–483.

[16] B. Yao, D.J. Edwards, R.J. Kurtz, TEM characterization of dislocation loops in irradiated bcc Fe-based steels, Journal of Nuclear Materials 434 (2013) 402–410.

[17] I.M. Robertson, M.L. Jenkins, C.A. English, Low-dose neutron-irradiation damage in α-iron, Journal of Nuclear Materials 108-109 (1982) 209–221.
[18] K.G. Field, X. Hu, K.C. Littrell, Y. Yamamoto, L.L. Snead, Radiation tolerance of neutron-irradiated model Fe–Cr–Al alloys, Journal of Nuclear Materials 465 (2015) 746–755.
[19] A. Prokhodtseva, B. Décamps, A. Ramar, R. Schäublin, Impact of He and Cr on defect accumulation in ion-irradiated ultrahigh-purity Fe(Cr) alloys, Acta Materialia 61 (2013) 6958–6971.
[20] M. Klimenkov, A. Möslang, E. Materna-Morris, Helium influence on the microstructure and swelling of 9%Cr ferritic steel after neutron irradiation to 16.3 dpa, Journal of Nuclear Materials 453 (2014) 54–59.
[21] Modern Physical Metallurgy, Elsevier, 2014.
[22] S.L. Dudarev, P.-W. Ma, Elastic fields, dipole tensors, and interaction between self-interstitial atom defects in bcc transition metals, Phys. Rev. Materials 2 (2018).
[23] A. Kimura, Current Status of Reduced-Activation Ferritic/Martensitic Steels R&D for Fusion Energy, Mater. Trans. 46 (2005) 394–404.
[24] M. Klimenkov, A. Möslang, E. Materna-Morris, H.-C. Schneider, Helium bubble morphology of boron alloyed EUROFER97 after neutron irradiation, Journal of Nuclear Materials 442 (2013) S52-S57.
[25] Z. Yao, M.L. Jenkins, M. Hernández-Mayoral, M.A. Kirk, The temperature dependence of heavy-ion damage in iron: A microstructural transition at elevated temperatures, Philosophical Magazine 90 (2010) 4623–4634.
[26] C. Dethloff, E. Gaganidze, J. Aktaa, Review and critical assessment of dislocation loop analyses on EUROFER 97, Nuclear Materials and Energy 15 (2018) 23–26.
[27] J. Gao, P. Song, Y.-J. Huang, K. Yabuuchi, A. Kimura, K. Sakamoto, S. Yamashita, Effects of neutron irradiation on 12Cr–6Al-ODS steel with electron-beam weld line, Journal of Nuclear Materials 524 (2019) 1–8.
[28] C. Sobie, N. Bertin, L. Capolungo, Analysis of Obstacle Hardening Models Using Dislocation Dynamics: Application to Irradiation-Induced Defects, Metall and Mat Trans A 46 (2015) 3761–3772.
[29] R.E. Stoller, S.J. Zinkle, On the relationship between uniaxial yield strength and resolved shear stress in polycrystalline materials, Journal of Nuclear Materials 283-287 (2000) 349–352.
[30] M. Sanctis, A. Fava, G. Lovicu, R. Montanari, M. Richetta, C. Testani, A. Varone, Mechanical Characterization of a Nano-ODS Steel Prepared by Low-Energy Mechanical Alloying, Metals 7 (2017) 283.
[31] L. Tan, J.T. Busby, Formulating the strength factor α for improved predictability of radiation hardening, Journal of Nuclear Materials 465 (2015) 724–730.
[32] R. Coppola, M. Klimenkov, Dose Dependence of Micro-Voids Distributions in Low-Temperature Neutron Irradiated Eurofer97 Steel, Metals 9 (2019) 552.
[33] R. Coppola, M. Klimenkov, A. Möslang, R. Lindau, M. Rieth, M. Valli, Micro-structural effects of irradiation temperature and helium content in neutron irradiated B-alloyed Eurofer97-1 steel, Nuclear Materials and Energy 17 (2018) 40–47.